Journal of
Applied Crystallography
ISSN 0021-8898

Received 22 August 2011
Accepted 18 November 2011

Investigation of indirect structural and chemical parameters of GeSi nanoparticles in a silica matrix by combined synchrotron radiation techniques

Antonio Gasperini,[a,b] Angelo Malachias,[a,c] Gilberto Fabbris,[a,b] Guinther Kellermann,[a,d] Angelo Gobbi,[a] Esteban Avendaño[a] and Gustavo de Medeiros Azevedo[a,e]*

[a]Laboratório Nacional de Luz Síncrotron, Campinas, SP, CP 6192 – CEP 13083-970, Brazil, [b]Instituto de Física Gleb Wataghin, Universidade Estadual de Campinas, Campinas, SP, CEP 13083-859, Brazil, [c]Departamento de Física, Universidade Federal de Minas Gerais, CP 702, Belo Horizonte, Minas Gerais, 30123-970, Brazil, [d]Departamento de Física, Universidade Federal do Paraná, Curitiba, PR, Caixa Postal 19091, 81531-990, Brazil, and [e]Instituto de Física, Universidade Federal do Rio Grande do Sul, Porto Alegre, CP 15051, 91501-970, Brazil. Correspondence e-mail: gustavo.azevedo@ufrgs.br

The formation of GeSi nanoparticles on an SiO_2 matrix is studied here by synchrotron-based techniques. The shape, average diameter and size dispersion were obtained from grazing-incidence small-angle X-ray scattering data. X-ray diffraction measurements were used to obtain crystallite sizes and composition *via* resonant (anomalous) measurements. By using these techniques as input for extended X-ray absorption fine structure analysis, the local composition surrounding the Ge atoms is investigated. Although the results for each of the methods above are commonly analyzed separately, the combination of such techniques leads to an improved understanding of nanoparticle structural and chemical properties. Crucial indirect parameters that cannot be quantified by other means are accessed in this work, such as local strain, the possibility of forming core–shell structures, the fraction of Ge atoms diluted in the matrix (not forming nanoparticles), the amorphous and crystalline Ge fractions, and the relative population of nanoparticles with single and multiple crystalline domains.

1. Introduction

Small clusters containing a few tens to thousands of atoms exhibit modified chemical and physical properties when compared with their bulk counterparts with the same chemical composition. Such differences arise mainly because of the great proportion of atoms composing the surface of the clusters (large surface/volume ratio) and because of electron spatial confinement, which affects the electronic structure, with consequences in chemical, optical and magnetic properties. Nanoparticles have been attracting much attention since it was realized that the reduction of dimensionality offers an alternative pathway to manipulate and control material properties, besides the more traditional control over chemical composition. Indeed, nanoparticles constitute novel materials, with a plethora of applications in diverse areas such as catalysis, spintronics and optoelectronics.

An important class of nanostructured systems are dielectric thin films containing semiconducting or metallic nanoparticles. Such thin films find potential applications in optoelectronics and information storage. For instance, metallic nanoparticles embedded in silica modify the dielectric optical properties, giving rise to linear (Dowd *et al.*, 2001) and nonlinear effects in the refraction index (Fukumi *et al.*, 1994; Lee *et al.*, 1997; Hamanaka *et al.*, 2004; Bernas, 2009), and enabling the production of transistor-like optical units, where a light beam could be controlled by another beam. Another remarkable property of this class of nanostructured materials can be found in group IV semiconductors, which are poor light emitters in bulk form but exhibit strong luminescence in the form of nanometric clusters embedded in dielectrics (Maeda, 1995; Pavesi *et al.*, 2000; Rebohle *et al.*, 2000). The preparation of Si and Ge nanoparticles encapsulated in silica is entirely compatible with the existing microelectronics industry, and could open up the possibility of Si-based optical devices for light generation, modulation and processing, with great potential for applications in telecommunications and data processing. More recently, it has been demonstrated that nanoparticles (either metallic or semiconductor) embedded in thin dielectric films exhibit reversible charge storage properties, with applications in the fabrication of nonvolatile memory devices (Park *et al.*, 2006; Tsoukalas *et al.*, 2005).

Thin films containing nanoparticles can be obtained by several preparation methods, including physical evaporation

(co-sputtering, thermal co-evaporation) or ion implantation, followed by thermal annealing (Maeda, 1995; Pavesi *et al.*, 2000; Rebohle *et al.*, 2000; Kolobov *et al.*, 2003; Zhang *et al.*, 2010; Cheung *et al.*, 2004). To explore the potentialities of nanoparticles, a thorough understanding of the influence of preparation conditions on the final chemical and structural properties is required. However, this step can be hampered by some peculiarities of nanoparticles that make their structural characterization a challenging task. Firstly, the long-range order characteristic of crystalline materials is truncated as a result of their reduced dimensionality. Secondly, nanostructures tend to be highly disordered (Cheung *et al.*, 2004; Rockenberger *et al.*, 1998; Ridgway *et al.*, 2004), given the lesser constraints on the positions of surface atoms owing to reduced coordination and/or interactions with the surrounding matrix. Hence, well established techniques developed for crystallography are of limited application (Billinge & Levin, 2007). In compound nanoparticles, the problem of structural determination is even more complicated, requiring chemically selective structural determination. In this sense, the usual approach to nanostructure characterization involves a combination of several techniques, covering structure, morphology and chemical composition.

In this paper, we highlight the importance and utility of synchrotron radiation-based techniques such as extended X-ray absorption fine structure spectroscopy, grazing-incidence small-angle X-ray scattering and anomalous X-ray diffraction in the characterization of nanostructures. This suite of techniques yields information on several length scales, in both real and reciprocal space, with chemical selectivity, producing a complete picture of the structural properties of the nanoparticle system under study. For the purpose of this paper, the system of choice is Ge_xSi_{1-x} nanoparticles embedded in silica, prepared *via* co-sputtering of silica and germanium. This system presents several of the challenges that a materials scientist would face in the characterization of nanostructures: an initially unknown composition, polydispersity, strain/stress, and mixed amorphous and crystalline populations, to mention just a few. Although the results presented herein illustrate the potential of such a combination of synchrotron techniques in the analysis of only one material system, we think that our procedures are general enough to be directly applied to other nanostructured materials.

This manuscript is organized as follows: in §2 we describe our experimental methods and analysis procedures. In §3 we present our data and discuss the results separately. Finally, in §4, we confront the results obtained by different techniques and discuss the key role of synchrotron-based methods in the study and development of nanostructured materials. §5 is dedicated to general conclusions.

2. Experimental

SiO_2 films doped with Ge atoms were prepared by co-sputtering at the Brazilian Synchrotron Laboratory (LNLS) thin-films facility. Si(111) substrates were used as support for the sputtered films obtained using a Leybold Z-400 RF sputtering system with argon plasma. The deposition sequence for the samples studied here followed three steps. Initially an SiO_2 layer of 0.4 μm thickness was deposited by sputtering of an SiO_2 target. In the next step pieces of a pure Ge commercial wafer were arranged on top of the SiO_2 target and co-sputtered over the first SiO_2 layer, forming an 0.8 μm-thick layer. The effective area of the SiO_2 target surface covered by Ge wafer pieces (about 8% of the surface) provides a large amount of Ge – about 12% in volume – co-sputtered in the SiO_2 film at this step of the process. The Ge concentration (by volume) was determined from the X-ray absorption edge step in transmission-mode XAFS measurements of the studied samples (the layer thickness used to obtain the Ge concentration by the absorption step was calibrated by ellipsometry and electron microscopy). Finally, the Ge wafer pieces were removed from the sputtering chamber, allowing for the deposition of a 0.4 μm-thick SiO_2 layer on top of the previous layers. In such a sample layout the undoped SiO_2 films act as support for the doped films, as well as a barrier against the diffusion of Ge atoms from the doped layer to the substrate during annealing. This barrier avoids non-homogeneous Ge oxidation at the sample upper interface, which can happen if residual oxygen molecules are present in the sample annealing step (Vincent *et al.*, 2007). Ellipsometry measurements performed on calibration SiO_2 films sputtered by this method have shown that the obtained silica films were poor in oxygen, leading to a small deviation with respect to the stoichiometric compound.

In order to obtain Ge nanoparticles in the Ge-doped layer the samples were annealed at 1323 K in Ar atmosphere for 2 h. Such annealing induces a decomposition of the supersaturated SiO_2/Ge mixture by promoting the diffusion of Ge atoms, which agglomerate into nanometre-sized clusters, hereafter referred to as nanoparticles (NPs), inside the film. For a nonstoichiometric SiO_2 matrix, excess Si atoms may also diffuse inside the SiO_2 films, further contributing to the formation of NPs. The size of these NPs increases mainly with the annealing temperature, which activates and accelerates the diffusion process, and the annealing time, which allows for the migration and incorporation of atoms into larger Ge clusters (Lifshitz & Slyozov, 1961; Wagner, 1961).

High-resolution transmission electron microscopy (TEM) images of the sputtered as-deposited and annealed samples were obtained using a Jeol 3010 microscope installed at the C2nano laboratory of the LNLS. Images for a sample annealed for 2 h are shown in Fig. 1. The overview of Fig. 1(*a*) shows SiO_2 films (labeled as I), the Ge-doped film (II) and the glue used for TEM preparation (III). The formation of NPs of about 50 Å diameter is clearly observed in the TEM image of Fig. 1(*b*), which depicts the interface between the Ge-doped film and the SiO_2 upper layer. A single nanoparticle is shown in Fig. 1(*c*), where the appearance of discrete lines indicates that the nanoparticles consist of crystalline atomic arrangements.

X-ray diffraction (XRD) and grazing-incidence small-angle X-ray scattering (GISAXS) measurements were performed at the LNLS XRD-2 beamline. This beamline is equipped with

an Si(111) monochromator and a (4 + 2)-circle diffractometer. The X-ray energy was fixed at the maximum photon flux energy (8000 eV) for measurements of two-dimensional GISAXS patterns and complete longitudinal XRD scans. Anomalous X-ray diffraction measurements were performed at energies close to the Ge *K*-absorption edge, providing information about the chemical composition of crystalline NPs.

In the GISAXS setup, represented schematically in Fig. 2, an X-ray-sensitive image plate with 200 µm pixel size was positioned perpendicularly to the incident beam at a distance of 0.777 m from the sample position. The X-ray incident angle α_i was set to 0.5°, above the angle of total external reflection from SiO_2 (0.21°), allowing a penetration depth of about 1 µm, which optimizes the scattering signal from the NPs. Besides the measurements performed on annealed samples, where the presence of NPs was observed by TEM, GISAXS measurements were also performed on as-deposited Ge-doped and as-grown SiO_2 films. Except at very small q_y values, in which the contribution of the reflected beam can be observed, the scattering intensities of these samples are weak and nearly independent of the scattering vector **q**, suggesting that no NPs are formed before thermal treatment. In our analysis, this contribution was subtracted from to the total scattering intensity of the annealed samples.

Extended X-ray absorption fine structure (EXAFS) measurements around the Ge *K*-edge (11 103 eV) were performed in fluorescence mode, utilizing a Canberra 15-element Ge detector, at the LNLS XAFS2 beamline, which is optimized for XAFS spectroscopy in the 4–18 keV energy range. The beamline optics consist of a cylindrical Rh-coated Si mirror for vertical collimation, an Si(111) double-crystal monochromator designed at LNLS, followed by a ULE Rh-coated bendable toroidal mirror for horizontal and vertical focusing. The beamline delivers a photon flux of $\sim 10^9$ photons s^{-1} in a 1.0 mm^2 spot in the energy range of the measurements. In order to avoid signal contamination due to Bragg peaks from the substrate, the samples analyzed by EXAFS were deposited onto commercial 1.5 × 1.5 mm, 0.5 µm-thick, self-supported amorphous Si_3N_4 substrates. During measurements, samples were mounted in a closed-circuit He cryostat, and the temperature was kept at 20 K and controlled within ±0.5 K tolerance. Energy steps and acquisition times were varied from 1 eV and 2 s in the pre-edge and X-ray absorption near-edge spectroscopy region to 2–3 eV and 4–6 s in the EXAFS region. Each measurement consisted of at least three scans. A crystalline Ge sample was also analyzed and served as a standard for EXAFS data analysis. This standard sample, optimized for transmission measurements, was obtained by finely crushing a piece of a Ge commercial wafer and depositing the powder onto milipore polyvinylidene difluoride membranes, in amounts calculated to yield an edge jump of around 1 near the Ge *K*-edge.

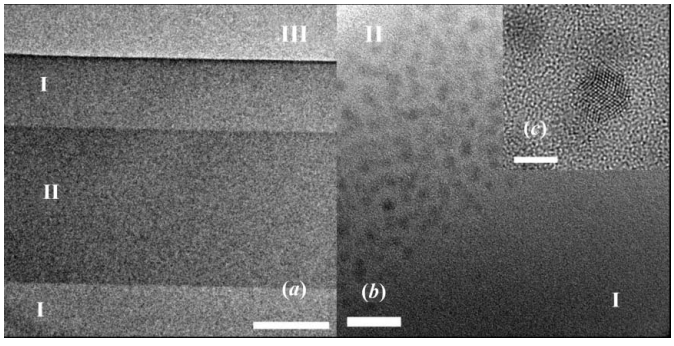

Figure 1
TEM images with different magnifications showing a sample produced by sputtering (see text) and annealed for 2 h in Ar atmosphere at 1323 K. The SiO_2 films are labeled as I in (*a*) and (*b*), while the film containing the Ge nanoparticles is labeled as II. The complete layer stack is shown in (*a*), where the glue is labeled as III. The interface between the SiO_2 and the SiO_2 film with Ge nanoparticles is shown in (*b*). A crystalline nanoparticle is seen in (*c*). Scale bars correspond to 0.4 µm in (*a*), 200 Å in (*b*) and 50 Å in (*c*).

Table 1
Parameters of the NP diameter distribution obtained by TEM – averaged over 173 nanoparticles – and GISAXS.

From both techniques the nanoparticle diameter D_0, distribution width σ and σ/D_0 ratio are shown. The parameters c, η_{HS} and D_{NP} are extracted from the GISAXS fit procedure discussed in §3.1.

	TEM	GISAXS
D_0 (Å)	61 (6)	55 (4)
σ (Å)	16 (2)	14 (3)
σ/D_0	0.27 (3)	0.26 (5)
c	–	1.10 (14)
η_{HS}	–	0.19 (2)
D_{NP} (Å)	–	113 (16)

3. Results and discussion

3.1. Grazing-incidence small-angle X-ray scattering

In this work, TEM was used to verify the formation of NPs, as shown in Fig. 1. As depicted in Figs. 1(*b*) and 1(*c*), the NPs formed after annealing of the sample exhibit spherical shapes and are crystalline at this stage of growth. By performing a statistical analysis over a large area of the sample containing 173 NPs we were able to extract the average nanoparticle diameter (D_0) and the size dispersion (σ), as shown in Table 1.

Although TEM results can directly show nanoparticle shapes and yield an average particle size *via* statistical analysis, it is a restricted technique with respect to the overall statistical behavior of the formed NPs. One must notice, for instance, that size distribution measurements obtained by TEM

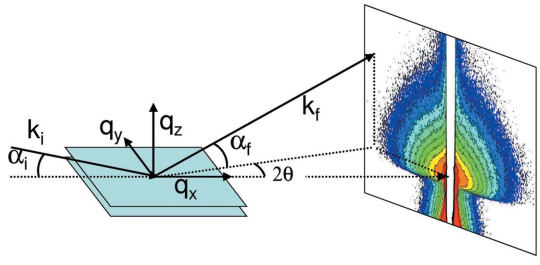

Figure 2
Schematic representation of the GISAXS setup, showing the components of the scattering vector **q**.

strongly depend on the thickness of the sample in the region in which a given statistical procedure is performed (Bonafos *et al.*, 2000). Such features can produce distinct differences between the averaged data obtained for different positions on the same sample. The lack of depth-resolved information may be responsible for the miscounting of overlapped particles aligned along the observation axis, as well as for obtaining a larger particle size during the delimitation of dark spots in images like Fig. 1(*b*). It is necessary, therefore, to use extremely narrow regions obtained during sample preparation, which do not have a sufficiently large extension over the specimen to allow for good statistics. Finally, TEM is inherently a destructive method, requiring sample preparation procedures that can modify the sample properties and render it unusable for measurements with other techniques.

In contrast, X-ray scattering techniques such as SAXS and GISAXS are able to probe an extremely large number of nanoparticles, allowing for a statistically precise determination of shape, size and size dispersion of particles. These techniques can also probe spatial correlations among particles, providing information on the average particle–particle distance. GISAXS and SAXS measurements can be performed in different sample environments, allowing for *in situ* observation of physical phenomena or chemical reactions that lead to sample formation. With the continuous radiation spectrum from a synchrotron light source, one can also perform anomalous (resonant) measurements at a given element absorption edge, obtaining chemical information on the studied nanostructures.

In particular, the GISAXS technique can be applied to study samples deposited on top of a thick substrate, without requiring sample preparation for standard SAXS transmission measurements. Furthermore, by tuning the X-ray beam incident angle α_i (shown in Fig. 2) one can probe different depths of the sample, allowing for measurements that span from surface/interface roughness to buried NPs for a thick film. Measurements in GISAXS geometry are also more accurate for describing nanostructure shapes in samples that are epitaxially oriented since the scattering vector component perpendicular to the surface direction (q_z) is well characterized (Rauscher *et al.*, 1999). In such cases, transmission SAXS measurements provide results with erroneous object symmetry.

In this work, we have applied the GISAXS technique to study the shape, size, size dispersion and particle–particle distance information. Since the samples were deposited on thick Si(111) substrates, GISAXS measurements have been shown to be the best option for studying the system without any requirement for sample preparation.

The GISAXS scattering vector components q_x, q_y and q_z represented in Fig. 2 can be correlated to the incident ($\mathbf{k}_i$) and scattered (exit, $\mathbf{k}_f$) photon wavevectors by

$$\mathbf{q} = \mathbf{k}_f - \mathbf{k}_i = \begin{pmatrix} q_x \\ q_y \\ q_z \end{pmatrix} = \begin{bmatrix} \cos(\alpha_f)\cos(2\theta) - \cos(\alpha_i) \\ \cos(\alpha_f)\sin(2\theta) \\ \sin(\alpha_f) + \sin(\alpha_i) \end{bmatrix}, \quad (1)$$

where α_i and α_f are the incident and exit angles with respect to the sample surface plane, respectively, and 2θ is the scattering angle with respect to the specular scattering plane. A Cartesian *xyz* axis system is oriented with respect to the sample surface and incident beam direction, with the *z* axis oriented along the surface normal direction and the *x* axis lying collinearly to the incident beam direction (see Fig. 2).

Since the NPs studied here were buried in an SiO_2 film, the X-ray refraction and reflection effects at the air/film interface must be taken into account to correctly describe the GISAXS intensity pattern. To account for this, the out-of-plane component of the scattering vector q_z must be replaced by $\tilde{q}_z = 2\pi[\sin_r(\alpha_i) + \sin_r(\alpha_f)]/\lambda$, where $\sin_r(\alpha) = (\sin^2\alpha - 2\delta + 2i\beta)^{1/2}$, and $1-\delta$ and β are the real and imaginary parts, respectively, of the SiO_2 index of refraction for the used X-ray energy (Paniago *et al.*, 1997).

Fig. 3(*a*) shows a two-dimensional GISAXS scattering pattern obtained with an image plate by performing measurements on samples containing Ge NPs (annealed) and the as-deposited Ge-doped SiO_2 sample (inset). The comparison of these two patterns directly shows the presence of nanoparticles in the annealed sample, while the as-grown Ge-doped sample shows a scattering pattern very similar to a reference thick SiO_2 film sample. This indicates that NPs are only formed after the annealing procedure, as corroborated by supplementary TEM measurements (not shown here; since both TEM and GISAXS measurements are unable to detect nanoparticles much smaller than $\sim$8 Å we cannot rule out completely the absence of very small clusters). The signal from the as-deposited reference sample is essentially a superposition of the reflected beam pattern with the scattering from the rough surface of the film. The vertical white stripes along q_z at $q_y = 0$ in these measurements are shadows produced by the beam stopper, positioned to avoid the saturation of the image plate by the incident and reflected beam.

In order to isolate the scattering signal of the NPs from the matrix background, the GISAXS pattern of a 1.2 µm-thick reference SiO_2 film is subtracted from the data measured on the sample with NPs shown in Fig. 3(*a*). Selected cuts of the corrected pattern, shown in Fig. 3(*b*), are then used for fitting with an appropriate model. The intensity *versus* q_y profiles, obtained for fixed q_z, are represented by the dots in Fig. 3(*b*). A careful analysis of the GISAXS result of Fig. 3(*a*) shows a small effect of correlation among particles for lower q_y and q_z values. This effect is more easily observed in the three cuts with lower q_z in Fig. 3(*b*), where it can be related to the decrease in scattering intensity at lower q_y values. Fig. 3(*c*) shows how the particle correlation affects the fit of the first cut in q_z (q_z = 0.0584 Å^{-1}). By simulating the same scattering profile without any correlation effects one notices that the intensity at small q_z–q_y values becomes larger than the observed data. Such a change cannot be counterbalanced by modifying any other parameter (including a scaling constant). Any attempt to fit the data without a correlation factor hence leads to a significantly worse matching between simulation and measurements at small q_y values. Moreover, the absence of oscillations or shoulders in the intensity profiles in the inter-

mediate q_y region suggests a rather large dispersion in nanoparticle sizes.

The constant-q_z profiles of Fig. 3(*b*) were fitted using the local monodisperse approximation (Pedersen, 1994), where the scattering amplitude is calculated as an incoherent sum of size-monodisperse subsystems, weighted by the overall nanoparticle size distribution. Such an approximation is generally applied to systems with large size dispersion and yields good results for such cases, in contrast to the decoupled approximation, which is better suited for low concentrations or low size polydispersity (Kotlarchyk & Chen, 1983; Renaud *et al.*, 2009). The GISAXS intensity equation used for the fits of Fig. 3(*b*) can be written as

$$I(q) = N \int_0^\infty |\Phi(q; D)|^2 S[q, D_{\rm HS}(D)] f(D)\, {\rm d}D, \qquad (2)$$

where Φ is the Born approximation form factor for a sphere (Renaud *et al.*, 2009), $S(q, D_{\rm HS})$ is the structure factor for hard spheres in the Percus–Yevick model (Percus & Yevick, 1958; Wertheim, 1963), $f(D)$ is the size distribution for the nanoparticle ensemble and N is a constant that accounts for all constant terms of equation (2) (incident beam intensity, illuminated area, number of scatterers *etc.*). In this model $D_{\rm HS} = cD$ is the diameter of closest approach of hard spheres, where c is a fitting parameter. The Percus–Yevick structure factor can be expressed as $S(q, D_{\rm HS}) = [1 + 24\eta_{\rm HS}G(q, D_{\rm HS})/(qD_{\rm HS})]^{-1}$, where $\eta_{\rm HS}$ is the volume fraction occupied by the hard spheres and $G(q, D_{\rm HS})$ is a function that accounts for correlations among two or more nanoparticles and is explained in detail by Kinning & Thomas (1984) and Pedersen (1994).

Morphological parameters such as the average diameter $\langle D\rangle$, the polydispersity σ, the diameter of closest approach of hard spheres $D_{\rm HS}$ (correlated to the parameter c) and the volume fraction of hard spheres $\eta_{\rm HS}$ were used as fit parameters in this work. Performing a simultaneous fit for the ensemble of constant-q_z cuts of Fig. 3(*b*) provides more reliable morphological parameters, since the parameter correlation is reduced. This procedure narrows down the error bars, leading to better results in comparison to fitting of individual

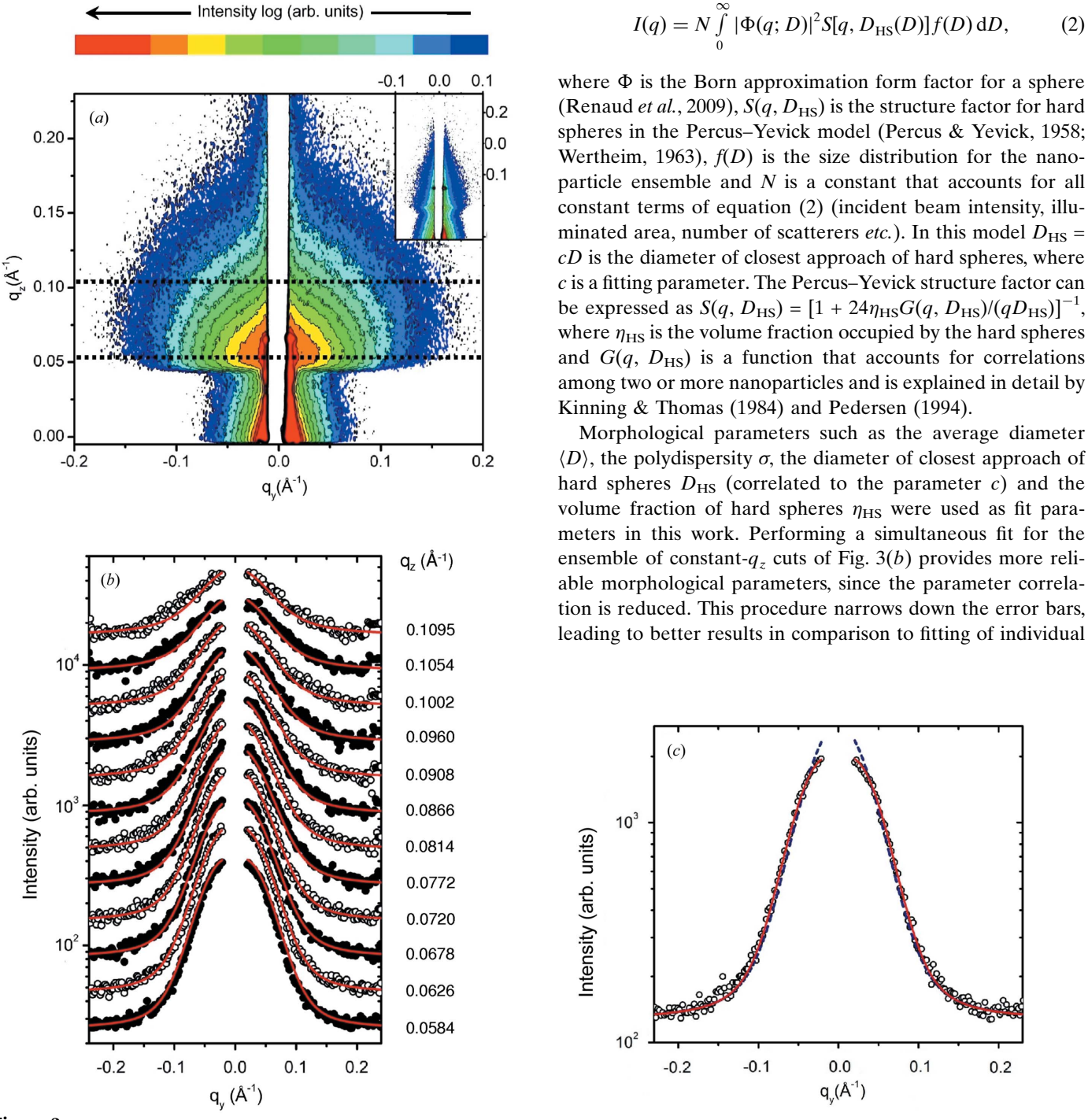

Figure 3
(*a*) Two-dimensional GISAXS scattering pattern captured in the q_yq_z plane by an image plate for the Ge nanoparticle sample (annealed for 2 h). The inset shows the GISAXS result for an as-deposited Ge-doped sample. The dotted lines in (*a*) represent the upper and lower q_z limits for the fittings shown in (*b*). (*b*) Fittings of selected constant q_z cuts from (*a*), using the model described in the text. (*c*) Nanoparticle correlation effect in the scattering intensity for the first constant-q_z (= 0.0584 Å^{-1}) cut of (*b*). Neglecting the correlation, the simulated profile overestimates the scattered intensity at low q_y (blue dashed curve). This effect cannot be obtained by any other parameter combination.

cuts. The parameters obtained for the best fit of the 2 h-annealed nanoparticle sample are listed in Table 1 and compared with TEM values.

3.2. Resonant and nonresonant X-ray diffraction

In order to verify whether the nanoparticles formed were crystalline we have performed XRD measurements on both as-grown and annealed samples. Fig. 4(*a*) shows longitudinal scans for both samples obtained at a fixed energy (8000 eV). The diffraction signal intensity was maximized for the 220 and 311 peaks by fixing the X-ray incident angle θ at 5°. Since nanoparticle lattices are randomly oriented, longitudinal scans were performed by varying solely the detector angle 2θ.

In Fig. 4(*a*) one observes the absence of peaks for the as-grown sample (lower curve), denoting that the undoped SiO_2 and Ge-doped SiO_2 layers are initially amorphous. After 2 h of annealing, three peaks, corresponding to 111, 220 and 311 reflections from the Ge crystalline structure, appear besides the large amorphous silica peak at q_r = 1.5 Å^{-1}. From the width of the 220 peak, further isolated from the inhomogeneous background from the amorphous SiO_2 matrix, one obtains an average crystallite size of 47 (5) Å. This inhomogeneous background does not allow for a quantitative estimation of the width of the crystallite size distribution using XRD data. In our size evaluation a Gaussian fit was performed, giving a peak width that results from the convolution of size, strain and instrumental broadening effects. In this case the width Δq_r is related to the size (Δq_{size}), strain (Δq_{strain}) and instrumental broadening (Δq_{inst}) by $\Delta q_r^2 = \Delta q_{size}^2 + \Delta q_{strain}^2 + \Delta q_{inst}^2$ (Revenant *et al.*, 2004). In our measurements the square of the size contribution to peak width is about 100 times larger than the other contributions, allowing for a direct evaluation of particle size from the measured line shape.

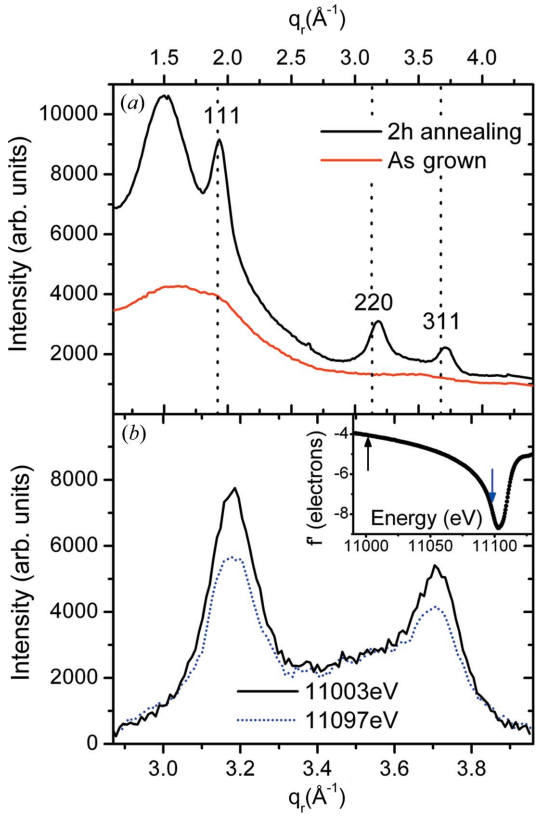

Figure 4
(*a*) X-ray diffraction longitudinal scans on an as-deposited sample (lower solid line) and on a sample annealed for 2 h under Ar atmosphere (upper/black solid line). Peaks corresponding to crystalline planes on the SiGe structure are indicated. Vertical dashed lines correspond to the expected positions of the diffraction peaks of a pure crystalline Ge reference measured at room temperature. (*b*) Anomalous X-ray diffraction in the vicinity of the 220 and 311 reflections at two energies close to the Ge *K*-edge: 11 003 eV (solid line) and 11 097 eV (dotted line). The variation of the dispersion correction f' for the atomic scattering factor of Ge is shown in the inset. At these two energies the absorption correction f'' for Ge does not vary significantly, while the Si atomic scattering factor remains constant (see text for details).

The position of all measured diffraction peaks clearly indicates a contraction of the lattice of about 1.1% with respect to bulk Ge. Such contraction can be due to diffusion of Si atoms as a result of stoichiometric deviations on the silica matrix, leading to the incorporation of Si atoms in alloyed nanoparticles, or due to strain/stress from the interface between each nanoparticle and the surrounding silica matrix. A solution to such apparent ambiguity is obtained by performing chemically sensitive anomalous X-ray diffraction in the vicinity of the Ge *K*-edge (11 103 eV).

Fig. 4(*b*) shows longitudinal scans in the vicinity of the 220 and 311 reflections at two selected energies, indicated in the inset. A significant variation of the dispersive correction (f') of the atomic scattering factor is obtained by comparing measurements performed at the two energies shown in Fig. 4(*b*). For these energies – 11 003 and 11 097 eV – the absorption correction f'' does not vary considerably and is much smaller than f' [here the dispersion correction f' was retrieved by performing a Kramers–Kronig transform on the Ge absorption data measured by fluorescence in the 2 h-annealed sample, according to Waseda (2002)], while the scattering of Si atoms is constant at this energy interval. The diffracted intensity measured at both reflections is then proportional to the square of the average atomic scattering factor, *i.e.* $I \propto \langle f_{GeSi}\rangle^2$. $\langle f_{GeSi}\rangle$ is the sum of Si and Ge atomic scattering factors, f_{Si} and f_{Ge}, respectively, weighted by the Si and Ge concentration (C_{Si} and C_{Ge}), $\langle f_{GeSi}\rangle = C_{Si}f_{Si} + C_{Ge}f_{Ge}$. Therefore, the ratio between diffracted intensities I_1 and I_2 measured at two energies can be written as

$$\frac{I_1}{I_2} = \left(\frac{C_{Ge}f_{Ge_1} + C_{Si}f_{Si}}{C_{Ge}f_{Ge_2} + C_{Si}f_{Si}}\right)^2, \qquad (3)$$

where f_{Ge1} and f_{Ge2} represent the scattering factors of Ge atoms at the two energies. Expressing C_{Ge} as a function of the other variables one obtains (Magalhães-Paniago *et al.*, 2002)

$$C_{Ge} = \left[1 + \frac{f_{Ge_2}I_1^{1/2} - f_{Ge_1}I_2^{1/2}}{f_{Si}(I_2^{1/2} - I_1^{1/2})}\right]^{-1}. \qquad (4)$$

Using the integrated area of the peaks of Fig. 4(*b*) as input to the intensities in equation (4) one obtains an average Ge

concentration of 0.62 (8) for the NPs. One must notice, however, that the existence of an inhomogeneous background below the 220 and 311 peaks strongly affects the composition results obtained from anomalous diffraction measurements. In epitaxial systems, where a peak from an Si reference crystal is present (Magalhães-Paniago *et al.*, 2002), an unambiguous matching of the curves obtained at different energies is straightforward, yielding quantitative concentration values. In our system, the absence of such a reference can introduce additional errors into the obtained Ge concentration, which is herein taken as semi-quantitative evidence for the incorporation of the Si atoms into the NPs. Using the 220 peak position, which indicates structurally the average lattice parameter a', one finds $a' = 5.587$ Å for our NPs. This lattice parameter corresponds to an unstrained Ge concentration of 0.71 (2) (Dismukes *et al.*, 1964; Kasper, 1995).

3.3. X-ray absorption spectroscopy

Although XRD measurements can reveal the behavior of crystallized material inside the NPs, such measurements are not able to provide information on the local vicinity of the Ge atoms, which undergoes strong changes from the amorphous to the crystalline state. EXAFS yields atomic level, chemically selective local structural information on interatomic distances, disorder (both structural and thermal) and average coordination numbers (Rehr & Albers, 2000; Lee *et al.*, 1981; Aksenov *et al.*, 2001). As abundantly demonstrated in the literature (Kolobov *et al.*, 2003; Cheung *et al.*, 2004; Rockenberger *et al.*, 1998; Ridgway *et al.*, 2004; Modrow, 2004; Frenkel *et al.*, 2001; Gilbert *et al.*, 2004; Rockenberger *et al.*, 1997; Araújo *et al.*, 2006; Araújo, Giulian *et al.*, 2008), EXAFS is particularly useful for the study of nanoparticles, given the typical photoelectron mean-free path of ∼10 Å, well matched to the dimensions of the NPs (Frenkel *et al.*, 2001).

Ge *K*-edge EXAFS measurements were performed as described in the *Experimental* section. Background subtraction and data processing were performed with the *ATHENA* code, part of the *IFEFFIT* and *Horae* software packages (Ravel & Newville, 2005).

The EXAFS signals of the bulk Ge standard (dotted line) and nanocrystals (solid line) are presented in Fig. 5(*a*). The signal-to-noise ratio in fluorescence mode for the sample containing NPs renders EXAFS oscillations measurable up to a photoelectron wavenumber $k = 16$ Å^{-1}. The magnitudes of the Fourier transforms (FTs) of the EXAFS signals from Fig. 5(*a*), taken in the k range from 3.5 to 13.7 Å^{-1}, are displayed in Fig. 5(*b*). We note that the NPs exhibit FT peaks characteristic of the Ge diamond structure up to 5.5 Å, indicating a high degree of local structural order. The differences in the magnitude of the FT of the first-shell peak for nanoparticles and bulk Ge are attributable to both stoichiometry and local disorder, as will be discussed below.

For EXAFS data analysis, we have employed multiparametric nonlinear least-squares fitting *via* the *IFEFFIT* code (Newville, 2001) with multiple-scattering and Gaussian disorder approximations. The phase and backscattering amplitude were calculated *ab initio* with the *FEFF6.0* code (Zabinsky *et al.*, 1995). All fits were performed in R space, with multiple k weighting, to minimize correlations between amplitude-related parameters. The amplitude reduction factor (S_0^2) and the threshold energy (E_0) were determined from the analysis of the bulk crystalline reference sample and held constant during analysis of the samples containing NPs. As demonstrated by Ridgway *et al.* (1999), bulk Ge is a suitable reference for the determination of S_0^2 and E_0 in GeSi alloys. To further minimize the number of free parameters during structural refinement, the coordination numbers were fixed during the fits, as explained below.

The NPs contain undercoordinated atoms close to the surface, reducing the average coordination numbers probed by EXAFS as compared to the bulk counterpart with the same composition. This reduction is more pronounced for more distant coordination shells, as revealed by the average coordination numbers calculated for a spherical Ge nanoparticle as a function of the nanoparticle radius, presented in Fig. 6.

From GISAXS, we obtained the size distribution of approximately spherical NPs. Therefore, the average coordination numbers can be obtained by averages of the curves from Fig. 6 over the size distribution obtained by GISAXS and, subsequently, can be fixed during the EXAFS data analysis, avoiding correlations with disorder parameters. Taking into account the GISAXS size distribution in the

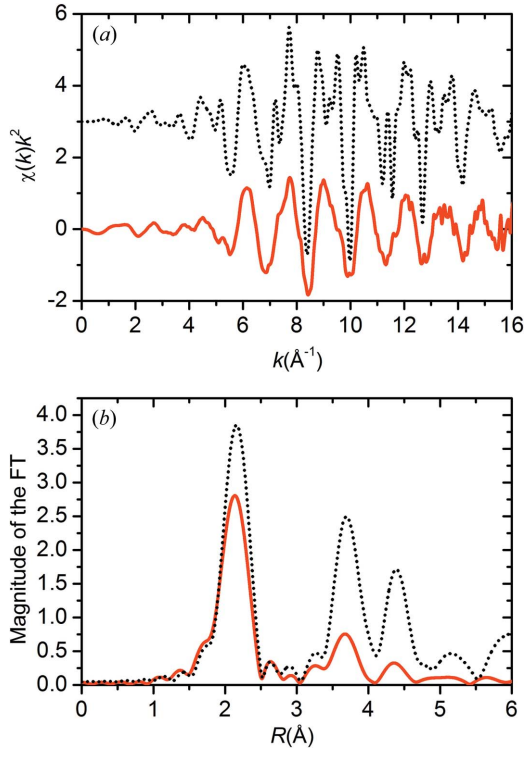

Figure 5
(*a*) k^2-weighted EXAFS signal (χ), as a function of the photoelectron wavenumber (k). The solid line corresponds to the spectrum of the sample containing nanocrystals. The dashed black line corresponds to the bulk Ge standard. The signal for the standard has been offset vertically for clarity. (*b*) Magnitude of the Fourier transforms of the signals shown in (*a*).

analysis yields the following average coordination numbers for the first three coordination shells of our nanoparticles: 3.77, 10.88 and 10.63. In the present case, the average coordination numbers are essentially the same as the values obtained by simple inspection of Fig. 6, considering the GISAXS diameter quoted in Table 1. However, very distinct values can be obtained in the analysis of small nanoparticles (diameter < 20 Å).

The fittings were performed in two steps. In the first step, only the first coordination shell was analyzed to obtain the nanoparticle composition, besides the structural parameters. In the following step, the analysis was extended to more distant shells, and the first, second and third coordination shells were analyzed simultaneously, yielding structural parameters and crystalline fraction. The structural parameters and composition parameters obtained for the first coordination shell are the same (within error bars) for both analysis procedures.

3.3.1. First-shell analysis. As indicated by a semi-quantitative anomalous diffraction composition estimation, our NPs consist of a Ge_xSi_{1-x} alloy with $x = 0.62\,(8)$. Supposing a GeSi random alloy, our fitting model for the first coordination shell thus includes single scattering paths from Ge and Si backscatterers. Owing to the complete overlap of the Ge–Si and Ge–Ge paths in *R* space (see Fig. 7*a*), a single Debye–Waller factor (DWF) was assigned to these paths. Such a constraint has been utilized by other authors in the analysis of crystalline GeSi alloys (Ridgway *et al.*, 1999; Aldrich *et al.*, 1994) and can be theoretically justified (Keating, 1996). The Ge–Ge and Ge–Si interatomic distances and sample composition were floated freely with the total coordination number fixed at a value of 3.77, corresponding to the average first-shell coordination number for spherical nanoparticles with the size distribution determined from the GISAXS measurements, as explained above.

Several EXAFS studies of structurally disordered elemental materials, such as amorphous semiconductors (Glover *et al.*, 2001) and nanostructures (Araújo *et al.*, 2006; Frenkel *et al.*, 2001), have highlighted the importance of inclusion of a third cumulant (*C*3), to properly account for static disorder-induced asymmetry of the interatomic distance distribution. *C*3 and the bond lengths are both related to the phase of the EXAFS signal and, therefore, are strongly correlated. Neglecting the third cumulant in the analysis of the first shell of structurally disordered elemental materials usually results in unphysically short bond lengths (Frenkel *et al.*, 2001). The necessity of a third cumulant is not so evident, though, in the analysis of compound materials with a mixed first shell, such as GeSi alloys. As we have checked, assuming the constraint of a common *C*3 associated with the first-shell Ge–Si and Ge–Ge paths does not significantly improve the fitting over that obtained including only up to the second cumulant (Debye–Waller factor). In the latter case, the values for *C*3 converge to values around zero, with large error bars. We ascribe such results to the fact that the overall GeSi interatomic distribution is intrinsically asymmetric owing to the presence of a short Ge—Si bond (2.37 Å) and a longer Ge—Ge bond (2.45 Å), hampering the observation of subtle bond-length asymmetries usually determined from the analysis of the third cumulant of the first coordination shell of elemental materials. We have thus ignored the third cumulant in our analysis. Overall, four fitting parameters are required to model the first coordination shell. The first-coordination-shell fits were performed in *R* space, in the 1.2–2.8 Å range. The parameters

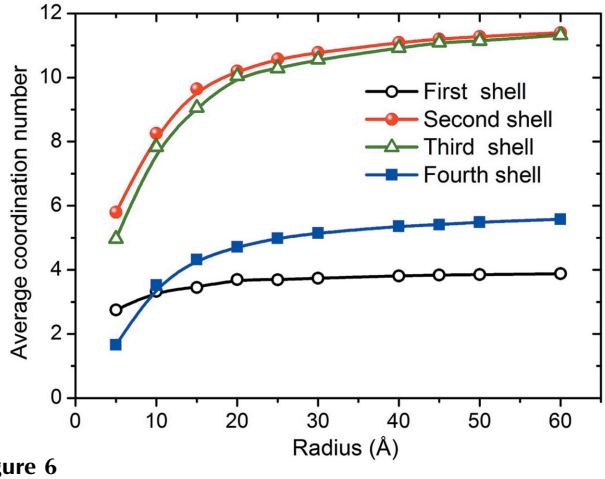

Figure 6
Calculated average coordination numbers for spherical Ge nanocrystals. The averages are performed over all atoms within a sphere of radius *R*. Atoms near the sphere surface exhibit reduced coordination, which is reflected in the variation of coordination number with radius.

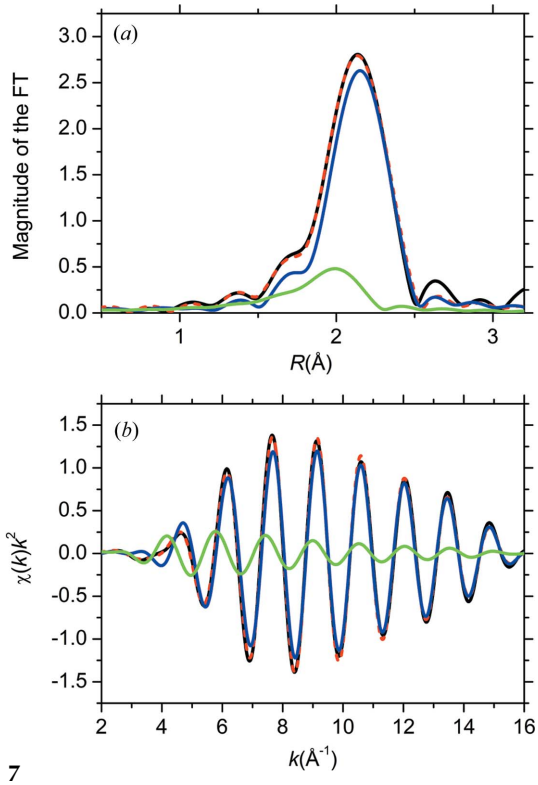

Figure 7
(*a*) Real-space fit of the first coordination shell (red dashed line) *versus* experimental data (black continuous line). The individual contributions of the Ge–Ge and Ge–Si paths correspond to the blue and green lines, respectively. (*b*) Back Fourier transforms of the peaks shown in (*a*).

Table 2
EXAFS fitting results: composition (x), crystalline fraction (α) and structural parameters for bulk standards and nanoparticles.

σ_n^2 denotes the Debye–Waller factors for the nth coordination shell, and R_{Ge-Ge} and R_{Ge-Si} are the Ge—Ge and Ge—Si interatomic distances, respectively. Parameters marked with an asterisk were fixed during the fittings. Two analysis procedures were utilized. In the first, only the first-coordination-shell signal was modeled. In the second, all coordination shells up to the third shell were included in the model. The structural parameters and composition parameters obtained for the first coordination shell are the same (within error bars) for both analysis procedures. Therefore, the figures quoted below refer to the extended procedure, including up to the third coordination shell.

Parameter	Bulk Ge	Ge_xSi_{1-x} NPs
x	1*	0.81 (2)
α	1*	0.81 (16)
First Shell		
σ_1^2 (Å^2)	0.0019 (1)	0.0023 (1)
R_{Ge-Ge} (Å)	2.448 (1)	2.441 (1)
R_{Ge-Si} (Å)	–	2.37 (1)
Second Shell		
σ_2^2 (Å^2)	0.0030 (2)	0.0066 (12)
R_{Ge-Ge} (Å)	3.998 (2)	3.951 (5)
R_{Ge-Si} (Å)	–	3.96 (3)
Third Shell		
σ_3^2 (Å^2)	0.0036 (2)	0.011 (2)
R_{Ge-Ge} (Å)	4.689 (2)	4.633 (5)
R_{Ge-Si} (Å)	–	4.64 (3)
E_0 (eV)	4.73 (3)	4.7*
S_0^2	0.97 (3)	0.97*

obtained in the fitting of the crystalline standard and nanoparticles are listed in Table 2.

In Fig. 7 we show the magnitude of the Fourier transform around the first coordination shell, where we compare the fit obtained with the experimental data for the nanocrystalline sample. The individual contributions of Ge–Ge and Ge–Si paths are also presented. The structural parameters corresponding to the fit in Fig. 7 are presented in Table 2.

3.3.2. Second-shell analysis. The analysis beyond the first coordination shell can provide further information on the structure of nanoparticles, as discussed below. This analysis requires inclusion of multiple scattering paths in the modeling of the EXAFS signal.

In the case of the bulk crystalline Ge, the fitting model to describe the signal in the R-space window from 1 to 4.7 Å requires inclusion of three single-scattering (S) paths (1, 3 and 5 in Table 3), two double-scattering (DS) paths (7 and 8) and one triple-scattering path (10; Sun *et al.*, 2005). The single- and multiple-scattering paths indicated in Table 3 are visualized in Fig. 8. The variation of path lengths can be conveniently constrained through the cubic structure of Ge and requires the inclusion of an overall expansion coefficient as a fitting parameter. An individual Debye–Waller factor was assigned to each single-scattering path. Given the complete R-space overlap between DS paths 7 and 8 and S path 3, the same Debye–Waller factor was assigned to paths 3, 7 and 8. The Debye–Waller factor for path 10 can be parameterized in terms of the S path 1 Debye–Waller factor. Coordination

Table 3
Schematic of the single- and multiple-scattering paths included in the analysis of the Ge bulk standard and GeSi nanocrystals.

Only paths with relative amplitude greater than 3% of path No. 1, as determined by *FEFF*, were included in the fits. Ge^n and Si^n denote backscatterers at the nth coordination shell. Ge^0 denotes the central atom.

Path No.	Path	R_{path} (Å)	Relative amplitude
Single Scattering			
1	$Ge^0 \rightarrow Ge^1 \rightarrow Ge^0$	2.45	1
2	$Ge^0 \rightarrow Si^1 \rightarrow Ge^0$	2.45	0.34
3	$Ge^0 \rightarrow Ge^2 \rightarrow Ge^0$	4.001	1
4	$Ge^0 \rightarrow Si^2 \rightarrow Ge^0$	4.001	0.074
5	$Ge^0 \rightarrow Ge^3 \rightarrow Ge^0$	4.691	0.650
6	$Ge^0 \rightarrow Si^3 \rightarrow Ge^0$	4.691	0.045
Multiple Scattering			
7	$Ge^0 \rightarrow Ge^1 \rightarrow Ge^1 \rightarrow Ge^0$	4.450	0.033
8	$Ge^0 \rightarrow Ge^2 \rightarrow Ge^1 \rightarrow Ge^0$	4.450	0.169
9	$Ge^0 \rightarrow Ge^2 \rightarrow Si^1 \rightarrow Ge^0$	4.450	0.063
10	$Ge^0 \rightarrow Ge^1 \rightarrow Ge^0 \rightarrow Ge^1 \rightarrow Ge^0$	4.900	0.038

numbers and path degeneracies were fixed at the crystalline bulk values. A total of six fitting parameters are required to model the bulk crystalline Ge standard.

The modeling of the EXAFS signal of the GeSi nanocrystals follows a similar approach, requiring inclusion of additional single- and multiple-scattering paths accounting for Ge and Si backscatterers (paths 2, 4, 6 and 9 in Table 3). In this case, a random GeSi alloy was assumed (Ridgway *et al.*, 1999; Aubry *et al.*, 1999) and the path amplitudes were parameterized in terms of the sample composition and average coordination numbers determined from the GISAXS size distribution. Inclusion of multiple-scattering paths is mandatory in the analysis of Ge nanoparticles for a thorough determination of amplitude-related parameters associated with the second and third coordination shells (Araújo, Foran *et al.*, 2008). Although bond-angle distortion is likely to reduce the significance of multiple scattering in the EXAFS analysis, this effect has only

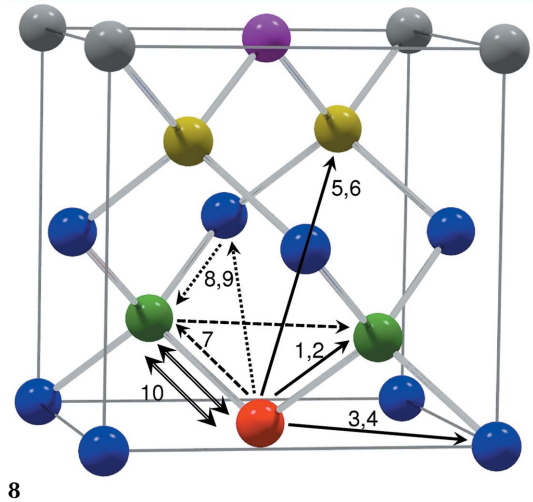

Figure 8
Single- and multiple-scattering paths included in the analysis of the Ge bulk standard and GeSi nanocrystals Paths lengths and relative amplitudes are indicated in Table 3. The absorbing atom is indicated in red. The first, second, third and fourth neighbors are drawn in green, blue, yellow and purple, respectively.

been considered indirectly, *via* the Debye–Waller factors of the multiple-scattering paths, which were parameterized in terms of the Debye–Waller factors of the single-scattering paths. As in the analysis of bulk Ge, overlapping paths in R space were assigned the same Debye–Waller factor. Unlike the pure crystalline Ge standard, the path distances cannot be constrained through a single expansion coefficient. Herein, three expansion coefficients were utilized to constrain the path lengths associated with first, second and third peaks in the Fourier transform of the EXAFS signal.

The differences in the average nanoparticle size obtained by GISAXS and XRD are indicative that some fraction of the Ge atoms have condensed in amorphous or amorphous-like environments. Previous EXAFS measurements provided experimental evidence for the presence of amorphous and crystalline environments in Ge nanoparticles encapsulated in silica (Araújo, Giulian *et al.*, 2008). From the analysis of amorphous semiconductors, it is well known that the first shell dominates the EXAFS signal, without coherent scattering from beyond the first shell. Indeed, one distinct feature of amorphous tetrahedral semiconductors is the absence of EXAFS signal beyond the first coordination shell (Ridgway *et al.*, 1999; Glover *et al.*, 2001; Azevedo *et al.*, 2002, 2003). Therefore, only the fraction of Ge atoms in crystalline environments contribute to the signal corresponding to the second and third coordination shells. The presence of an amorphous fraction, the reduced coordination due to surface truncation in the NPs, structural disorder and chemical composition are the contributing factors for the reduction in magnitude of the FT peaks for the second and third coordination shells relative to the bulk Ge standard, as noted previously in the presentation of the data shown in Fig. 5(*b*).

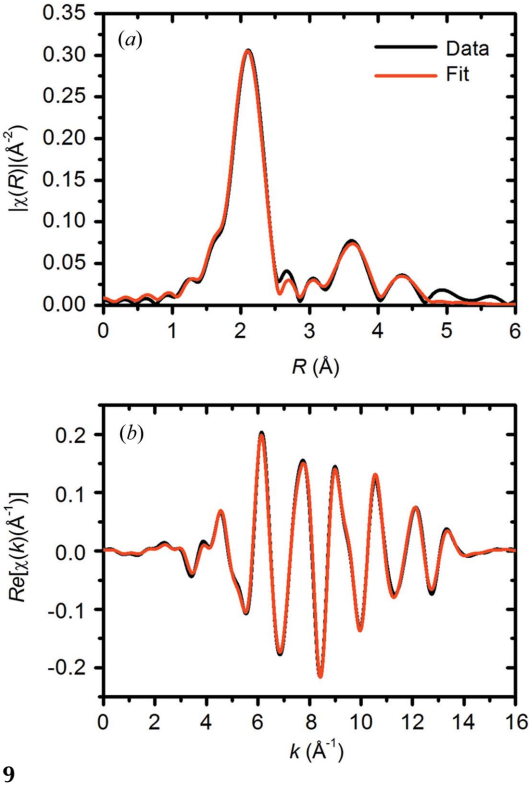

Figure 9
(*a*) FT of the k-weighted EXAFS signal (χ) (black line) and best fit (gray line; red in the electronic version of the journal) obtained with the model described in the text. (*b*) Filtered back Fourier transformed signals from (*a*), over the R-space fitting window (1.0–4.7 Å).

Assuming that a fraction α of the Ge atoms are surrounded by a crystalline environment, the EXAFS signal $\chi(k)$ can be modeled as $\chi(k) = \alpha\chi_{\rm crystal} + (1-\alpha)\chi_{\rm amorph}$, where $\chi_{\rm crystal}$ and $\chi_{\rm amorph}$ are the contributions from crystalline and amorphous environments, respectively. Both components contribute to the signal of the first shell, but only $\chi_{\rm crystal}$ contains information relative to the second and third coordination shells. Thus, we have included two possible environments in the modeling of the EXAFS signal of GeSi NPs.

The fitting results utilizing the model described above are presented in Fig. 9 and Table 2. A very good agreement between the best fit curve and the experimental spectrum is observed in both real (Fig. 9*a*) and k space (Fig. 9*b*).

As revealed by the structural parameters presented in Table 2, a significant fraction of the Ge atoms (81%) are surrounded by an essentially crystalline environment whilst the fraction sitting in amorphous environments is 19%. The amorphous fraction determined by EXAFS suggests that diluted Ge atoms and small amorphous clusters, not detectable by GISAXS and XRD, may still be present in the sample.

It is important to mention that the two analysis steps utilized firstly assure the mixed GeSi composition (first-shell analysis) and secondly assure that the amorphous fraction and the composition obtained by the full three-shell analysis are not compromised by correlations between amplitude-related parameters. The structural parameters and composition parameters obtained for the first coordination shell are the same (within error bars) for both analysis procedures. Therefore, the figures quoted in Table 2 refer to the extended procedure, including up to the third coordination shell.

4. Outlook

In order to bring the results from the previous sections into a common frame we explore in this section the possibility of cross-correlating results from the used techniques and evaluating aspects that could not be quantified by a single method. Initially one must comment on the Ge concentration figures for the NPs obtained from XRD and EXAFS. The composition obtained by EXAFS [x = 0.81 (2)] disagrees with the composition estimated from the lattice parameter obtained in our XRD measurements [x = 0.62 (8)]. XRD can determine the lattice parameter with great accuracy and, for the NPs studied herein, the lattice parameter a = 5.587 Å, which corresponds to a composition x = 0.71 (2) (Dismukes *et al.*, 1964; Kasper, 1995). Given that the lattice parameters of the GeSi alloys increase with Ge content, the composition obtained by EXAFS and the lattice parameter obtained by XRD can be reconciled if one considers the possibility that the NPs are subject to compressive strain. Indeed, *in situ* XAFS experiments demonstrate that our nanoparticles are molten during the high-temperature plateau of the annealing process and crystallize during cooling (A. Gasperini, in preparation).

The density of liquid Ge is 5% larger than the density of solid (crystalline or amorphous) Ge: $\rho_l \simeq 5.60\ \mathrm{g\ cm^{-3}}$ and $\rho_s = 5.32\ \mathrm{g\ cm^{-3}}$, respectively. Thus, an unconstrained NP would expand upon cooling from the molten phase. Despite the mismatch between the thermal expansion coefficients for silica and pure Ge (the former being one order of magnitude smaller than the latter) the expansion of the NPs due to the liquid–solid transition is not counterbalanced by the thermal contraction on cooling from the molten phase. Thus, a matrix-induced compressive strain of 0.5% could well be possible, conciliating the apparent inconsistency between the lattice parameter obtained by XRD and the sample composition obtained by EXAFS.

We note the good agreement between the interatomic distances measured herein and the interatomic distances measured in bulk GeSi alloys of similar composition [x = 0.81 (2)] (Ridgway *et al.*, 1999; Aldrich *et al.*, 1994; Yonenaga & Sakurai, 2001; Aubry *et al.*, 1999). Comparing the Debye–Waller factors for NPs and bulk standard, we note that in the first coordination shell both samples exhibit comparable disorder. However, the NPs contain significantly higher disorder in the second and third shells. The agreement between our bond-length measurements and higher disorder in the second and third shells leads us to conclude that, in the encapsulated GeSi NPs, a matrix-induced compressive strain would be mainly accommodated by bond-angle and dihedral-angle distortions, rather than bond-length distortions, which should be expected since bond-bending distortions are energetically favored over bond-stretching distortions in covalent semiconductors (Keating, 1996).

The parameters c and η_{HS} retrieved from GISAXS analysis allow for calculating the average distance between nanoparticles (D_{NP}) in our system. This distance can be obtained as

$$D_{NP} = cD_0 \exp(\sigma^2/D_0^2)/\eta_{HS}^{1/3}, \tag{5}$$

leading to a value of 113 (16) Å (see Appendix *A* for details). This distance can be used to infer the remaining Ge concentration in the matrix.

In order to estimate the number of Ge atoms diluted into the SiO_2 matrix after annealing, one has to consider the limiting case where all Ge atoms are located inside the NPs. In such conditions, the expected average distance between particles could be retrieved as $D_{NP} = D_0/C_{Ge}^{1/3}$, where C_{Ge} is the Ge concentration of the system, here considered as completely incorporated into the NPs. Since in our samples the integrated Ge content obtained in the sputtering process is equal to 0.12 (from X-ray absorption), the expected average distance between nanoparticles would be $\sim 2D_0$, which in our sample corresponds to 110 Å.

The combined results from the previous paragraphs indicate that a considerable amount of Ge is still diluted in the SiO_2 matrix after annealing. As shown before, the studied nanoparticles are an alloy of Si and Ge atoms, with about 20% Si composition. Hence, combining results from XAFS and GISAXS, the Ge concentration in the matrix (C_{Ge}^{M}) can be extracted as a function of the Ge concentration inside the NPs (C_{Ge}^{NP}), the total Ge concentration (C_{Ge}), and the parameters η_{HS} and c as

$$C_{Ge}^{M} = (C_{Ge} - C_{Ge}^{NP}\eta_{HS}/c^3)/(1 - \eta_{HS}/c^3). \tag{6}$$

By substituting our results into the equation above one finds that the Ge content in the SiO_2 matrix is 0.005, which is equivalent to 4.5% of all Ge atoms that were initially dissolved in the matrix. The extraction of C_{Ge}^{M} by the above-mentioned method is inherently lacking in precision, since the error bar calculation will take into account the error bar of NP concentration, which varies among the methods explored in this work. For our values, considering an error bar of 9% for C_{Ge}^{NP} leads to a 0.02 error bar in C_{Ge}^{M}. If the Ge concentration extracted from different methods had converged to very similar values, the error bar in C_{Ge}^{M} would reduce. The reduced Ge concentration inside the matrix in contrast to the Ge-rich NPs of the annealed sample explains why the signal corresponding to Ge—O bonds is not observed in the EXAFS signal for measurements in the sample with NPs.

Even though TEM and XRD size estimations are in agreement with GISAXS results (error bars overlap), one should not expect, in principle, agreement between these techniques. Firstly, we recall that XRD probes the average size of crystalline domains whilst GISAXS is sensitive to both amorphous and crystalline clusters. Secondly, the NP size evaluation is affected by the morphological properties of the NPs as discussed below. As revealed by the parameters from EXAFS presented in Table 2, a significant fraction of the Ge atoms (81%) are surrounded by an essentially crystalline environment, whilst 19% of the Ge atoms sit in an amorphous environment. This amorphous fraction can be explained on the basis of two different morphological models for the NPs. Both models are inspired by molecular dynamics (MD) simulation studies on the growth of pure Ge nanoclusters in silica (Bording & Tafto, 2000), which show that the interactions at the NP–matrix interface induce a significant structural disorder in the NPs. In the first model, it is assumed that matrix-induced structural disorder is homogeneously distributed over the volume of the NPs. Thus, in this model, one attributes the amorphous fraction to the presence of amorphous and crystalline populations in the NP ensemble. NPs with diameters greater than a critical diameter (D_c) would be fully crystalline, while smaller nanoparticles would be completely amorphous. The critical diameter can be obtained from the size distribution determined from GISAXS and the crystalline fraction determined from EXAFS (f_{cryst}) as

$$\int_{D_c}^{\infty} f_{vol}(D)\,\mathrm{d}D = f_{cryst}, \tag{7}$$

where $f_{vol}(D)$ is a distribution yielding the number of atoms in an NP of diameter D, which can be obtained from the GISAXS distribution $f(D)$ as

$$f_{vol}(D) = \frac{f(D)D^3}{\overline{D}^3 \exp[9\sigma^2/(2\overline{D}^2)]}, \tag{8}$$

Performing the indicated integration yields a critical diameter D_c = 40 Å, suggesting that NPs with a diameter smaller than 40 Å are amorphous. Clearly, such a morphological model would imply that the diameter estimation from XRD would yield larger average values than the estimated values from GISAXS, because NPs with diameters smaller than D_c are not probed by XRD and are not accounted for in the average diameter.

Bording and Tafto's theoretical MD predictions indicate that the matrix-induced structural disorder builds up within a transition layer between the NP–matrix interface and the NP crystalline core. A second structural model consistent with the amorphous fraction observed by EXAFS and the theoretical MD predictions would be a crystalline core surrounded by an amorphous shell. Previous XAFS work has provided experimental evidence for a core–shell structure in pure Ge NPs encapsulated in silica (Araújo, Giulian *et al.*, 2008). Clearly, such a core–shell model implies that larger average diameter values are obtained by GISAXS than by XRD. Bording & Tafto obtained a 10 Å thickness for the transition layer between the NP–SiO_2 interface and the crystalline core. Applying the theoretical prediction above to the core–shell model for a 47 Å-diameter crystalline core (as determined from XRD) results in nanoparticles with a 67 Å diameter. This would imply a crystalline fraction of 34% (66% amorphous fraction). These figures based on the comparison between our XRD measurements and theoretical MD predictions are clearly inconsistent with our EXAFS estimation of an 81% crystalline fraction.

The amorphous fraction can also be estimated by taking the central experimental diameter values obtained from XRD (47 Å) and GISAXS (55 Å) as the crystalline core and NP diameters, respectively. In this case, the amorphous shell would be 4 Å thick, and one finds that a possible amorphous shell would constitute roughly 38% of the volume of an average NP. The amorphous fraction obtained from the XRD–GISAXS comparison is roughly twice the amorphous fraction estimated from EXAFS. However, it can be taken as an upper bound for the amorphous fraction considering a core–shell model since it has been tacitly assumed that the NP crystalline core is composed of a single crystalline domain. NPs with more than one crystalline domain were observed in our system by TEM (see Fig. 1*c*, for instance). Because multiple domains within the same particle would not satisfy the Bragg reflection condition simultaneously, the average crystallite size measured by XRD must be smaller than the NP crystalline core diameter.

Reciprocally, the thickness of the amorphous shell can be estimated by considering the crystalline core diameter obtained by XRD and the amorphous fraction obtained by EXAFS. In this case, a ~2 Å-thick amorphous shell is obtained for the core–shell model. This value is smaller than a bond length and points, therefore, to the absence of a core–shell scenario. Since NPs with more than a single crystalline domain were observed by TEM, the latter comparison indicates an extremely reduced shell thickness, inconsistent with the MD theoretical predictions. The results obtained on a single sample in this work have hampered the identification of the best morphological model describing our GeSi NPs. Similar results obtained by our group in samples with different annealing times show that the evaluation of both structural and chemical parameters as discussed here is mandatory to build up a complete scenario for the growth of NPs.

It is worth commenting on the seeming inconsistency between the amorphous fractions determined from EXAFS and GISAXS–XRD results. Firstly, EXAFS and GISAXS–XRD probe atoms condensed within NPs, but the 4.5% of Ge atoms that remain dissolved in the matrix are probed only by EXAFS. Thus, the 62% crystalline fraction determined by GISAXS–XRD corresponds to 59% of all Ge atoms in the sample. The crystalline fractions of Ge atoms determined from scattering and absorption techniques do not agree within the error bars. The fact that some NPs are formed by more than one single-crystalline domain brings down the average D_{XRD} from XRD evaluation. Therefore, relying only on size evaluation through combined XRD–GISAXS does not lead to the correct value of crystalline fraction, which accounts for the deviation observed with respect to EXAFS. On the other hand, considering the EXAFS crystalline fraction as the correct one, we can estimate the population of NPs with multi-domain crystalline cores. Taking into consideration a simplified scenario in which the multi-domain NPs would happen to have only two crystallites each, the average diameter measured by XRD would be given by $D_{XRD} = D_0/(1 + p)$, where D_0 is the average diameter obtained by GISAXS and p is the fraction of NPs with multiple domains. In order to reach a crystalline fraction of 0.81 (EXAFS results) with a small population of multi-domain NPs with an average D_{XRD} of 47 Å, p has to fulfill the equality $[(1 + p) \times 47\ \text{Å}/55\ \text{Å}]^3 = 0.81$. This simplified calculation leads to $p = 0.09$, indicating that about 9% of the particles have more than one crystalline domain, in semi-quantitative agreement with our TEM results.

5. Conclusion

In this work, we have employed GISAXS, resonant and nonresonant XRD, and EXAFS to study the composition, morphology and structure of GeSi nanoparticles. Besides direct measurements, we have obtained important indirect results only accessible by combining the results of the various techniques. Our main conclusions can be summarized as follows. By combining EXAFS and GISAXS, we determined the Ge concentration in the matrix; the nanoparticle composition was obtained by EXAFS and anomalous XRD; comparing XRD and EXAFS, we determined the presence of compressive strain in the nanoparticles. Finally, the fraction of Ge atoms located in amorphous and crystalline environments and the morphological properties of the nanoparticles were considered, including an estimation of the population of multi-domain NPs from the combined results from XRD, GISAXS and EXAFS. EXAFS, GISAXS and XRD probe the material over several length scales (atomic level, mesoscopic and long-range structure, respectively) with chemical selectivity, yielding a complete characterization of the nanoparticles.

Although the results presented herein illustrate the potential of such a combination of synchrotron techniques in the analysis of only one material system, these procedures are general enough to be directly applied to other nanostructured materials.

APPENDIX *A*

In order to obtain equation (5), which gives the average NP distance, one must consider the average volume in the matrix occupied by a single NP (V_m/NP), in terms of the GISAXS parameters. In this case

$$V_m/\mathrm{NP} = (\pi/6)c^3\langle D^3\rangle/\eta_{HS}, \quad (9)$$

where $\langle\rangle$ represents an average over the size distribution and D is the NP diameter. The average volume can be expressed as a function of an effective diameter $D_{NP}^3 = c^3\langle D^3\rangle/\eta_{HS}$. This effective diameter represents the average distance between nanoparticles.

For a lognormal size distribution as used for GISAXS analysis,

$$\langle D^3\rangle = D_0^3 \exp(3\sigma^2/D_0^2), \quad (10)$$

then

$$D_{NP} = (c/\eta_{HS}^{1/3})D_0 \exp(\sigma^2/D_0^2), \quad (11)$$

where D_0 is the average NP diameter and σ^2 is the size distribution obtained from GISAXS analysis.

The estimation of Ge concentration in the SiO_2 matrix is performed by considering that the total Ge volume in the sample V_{Ge} is the sum of Ge atoms in the matrix V_{Ge}^M and the Ge atoms in the NPs V_{Ge}^{NP} ($V_{Ge} = V_{Ge}^M + V_{Ge}^{NP}$). Dividing by the total sample volume V_{TOT}, one gets

$$C_{Ge} = V^{NP}C_{Ge}^{NP}/V_{TOT} + V^M C_{Ge}^M/V_{TOT}, \quad (12)$$

where C_{Ge} is the volumetric Ge content in the sample, $V^{NP}(V^M)$ is the total volume occupied by the NPs (matrix) and $C_{Ge}^{NP}(C_{Ge}^M)$ is the volumetric content of Ge inside the NPs (matrix). Writing equation (12) as a function of GISAXS parameters, we obtain

$$C_{Ge} = V^{NP}C_{Ge}^{NP} + V^{NP}(c^3/\eta_{HS} - 1)C_{Ge}^M/(V^{NP}c^3/\eta_{HS}), \quad (13)$$

where $V_{TOT} = V^{NP}c^3/\eta_{HS}$. Therefore, the obtained Ge content inside the matrix is expressed in its final form as

$$C_{Ge}^M = (C_{Ge} - C_{Ge}^{NP}\eta_{HS}/c^3)/(1 - \eta_{HS}/c^3). \quad (14)$$

C_{Ge} can be directly obtained from the EXAFS step (knowing the sample thickness), C_{Ge}^{NP} is extracted by XRD or EXAFS, and η_{HS} and c come from GISAXS fitting.

The authors wish to thank the Brazilian agencies CNPq and FAPESP for financial support, LNLS for concession of beam time at beamlines XRD2 and XAFS2, and Laboratório de Microscopia Eletrônica for the access to the transmission electron microscopy facilities. AM and GK acknowledge CNPq project 473695/2009-0.

References

Aksenov, V. L., Kuzmin, A. Y., Purans, J. & Tyutyunnikov, S. I. (2001). *Phys. Part. Nuclei*, **32**, 1–33.
Aldrich, D. B., Nemanich, R. J. & Sayers, D. E. (1994). *Phys. Rev. B*, **50**, 15026–15033.
Araújo, L. L., Foran, G. J. & Ridgway, M. C. (2008). *J. Phys. Condens. Matter*, **20**, 165210.
Araújo, L. L., Giulian, R., Sprouster, D. J., Schnohr, C. S., Llewellyn, D. J., Kluth, P., Cookson, D. J., Foran, G. J. & Ridgway, M. C. (2008). *Phys. Rev. B*, **78**, 094112.
Araújo, L. L., Kluth, P., Azevedo, G. de M. & Ridgway, M. C. (2006). *Phys. Rev. B*, **74**, 184102.
Aubry, J. C., Tyliszczak, T., Hitchcock, A. P., Baribeu, J.-M. & Jackman, T. E. (1999). *Phys. Rev. B*, **59**, 12872–12883.
Azevedo, G. de M., Glover, C. J., Ridgway, M. C., Yu, K. M. & Foran, G. J. (2003). *Phys. Rev. B*, **68**, 115204.
Azevedo, G. de M., Ridgway, M. C., Yu, K. M., Glover, C. J. & Foran, G. J. (2002). *Nucl. Instrum. Methods Phys. Res. Sect. B*, **190**, 851–855.
Bernas, H. (2009). Editor. *Materials Science with Ion Beams*, Topics in Applied Physics, Vol. 116. Berlin, Heidelberg: Springer.
Billinge, S. J. & Levin, I. (2007). *Science*, **316**, 561–565.
Bonafos, C., Garrido, B., Lopez, M., Perez-Rodriguez, A., Morante, J. R., Kihn, Y., Ben Assayag, G. & Claverie, A. (2000). *Appl. Phys. Lett.* **76**, 3962–3964.
Bording, J. K. & Tafto, J. (2000). *Phys. Rev. B*, **62**, 8098–8103.
Cheung, A., Azevedo, G. de M., Glover, C. J., Llewellyn, D. J., Elliman, R. G., Foran, G. J. & Ridgway, M. C. (2004). *Appl. Phys. Lett.* **84**, 278–280.
Dismukes, P., Ekstrom, L. & Paff, R. F. (1964). *J. Phys. Chem.* **68**, 3021–3027.
Dowd, A., Ellimann, R. G. & Luther-Davies, B. (2001). *Appl. Phys. Lett.* **79**, 2327–2329.
Frenkel, A. I., Hills, C. W. & Nuzzo, R. G. (2001). *Phys. Chem. B*, **105**, 12689–12703.
Fukumi, K., Chayahara, A., Kadono, K., Sakaguchi, T., Horino, Y., Miya, M., Fujii, K., Hayakawa, J. & Satou, M. (1994). *J. Appl. Phys.* **75**, 3075–3080.
Gilbert, B., Huang, F., Zhang, H., Waychunas, G. A. & Banfield, J. F. (2004). *Science*, **305**, 651–654.
Glover, C. J., Ridgway, M. C., Yu, K. M., Foran, G. J., Desnica-Frankovic, I. D., Clerc, C., Hansen, J. L. & Nylandsted Larsen, A. (2001). *Phys. Rev. B*, **63**, 073204.
Hamanaka, Y., Fukuta, K., Nakamura, A., Liz-Marzán, L. M. & Mulvaney, P. (2004). *Appl. Phys. Lett.* **84**, 4938–4940.
Kasper, E. (1995). *J. Cryst. Growth*, **150**, 921–925.
Keating, P. N. (1996). *Phys. Rev.* **145**, 637–645.
Kinning, D. J. & Thomas, E. L. (1984). *Macromolecules*, **17**, 1712–1718.
Kolobov, A. V., Wei, S. Q., Yan, W. S., Oyanagi, H., Maeda, Y. & Tanaka, K. (2003). *Phys. Rev. B*, **67**, 195314.
Kotlarchyk, M. & Chen, S.-H. (1983). *J. Chem. Phys.* **79**, 2461–2469.
Lee, M., Kim, T. S. & Choi, Y. S. (1997). *J. Non-Cryst. Solids*, **211**, 143–149.
Lee, P. A., Citrin, P. H., Eisenberger, P. & Kincaid, B. M. (1981). *Rev. Mod. Phys.* **53**, 769–806.
Lifshitz, I. M. & Slyozov, V. V. (1961). *J. Phys. Chem. Solids*, pp. 35–50.
Maeda, Y. (1995). *Phys. Rev. B*, **51**, 1658–1670.
Magalhães-Paniago, R., Medeiros-Ribeiro, G., Malachias, A., Kycia, S., Kamins, T. I. & Williams, R. S. (2002). *Phys. Rev. B*, **66**, 245312.
Modrow, H. (2004). *Appl. Spectrosc. Rev.* **39**, 183–290.
Newville, M. (2001). *J. Synchrotron Rad.* **8**, 322–324.
Paniago, R., Forrest, R., Chow, P. C., Moss, S. C., Parkin, S. S. P. & Cookson, D. (1997). *Phys. Rev. B*, **56**, 13442–13454.
Park, C. J., Cho, K. H., Yang, W.-C., Cho, H. Y., Choi, S.-H., Elliman, R. G., Han, J. H. & Kim, C. (2006). *Appl. Phys. Lett.* **88**, 071916.

Pavesi, L., Dal Negro, L., Mazzoleni, C., Franzò, G. & Priolo, F. (2000). *Nature* (*London*), **408**, 440–444.
Pedersen, J. S. (1994). *J. Appl. Cryst.* **27**, 595–608.
Percus, J. K. & Yevick, G. J. (1958). *Phys. Rev.* **110**, 1–13.
Rauscher, M., Paniago, R., Metzger, H., Kovats, Z., Domke, J., Peisl, J., Pfannes, H. D., Schulze, J. & Eisele, I. (1999). *J. Appl. Phys.* **86**, 6763–6769.
Ravel, B. & Newville, M. (2005). *J. Synchrotron Rad.* **12**, 537–541.
Rebohle, L., von Borany, J., Fröb, H. & Skorupa, W. (2000). *Appl. Phys. B Lasers Opt.* **71**, 131–151.
Rehr, J. J. & Albers, R. C. (2000). *Rev. Mod. Phys.* **72**, 621–654.
Renaud, G., Lazzari, R. & Leroy, F. (2009). *Surf. Sci. Rep.* **64**, 255–380.
Revenant, C., Leroy, F., Lazzari, R., Renaud, G. & Henry, C. R. (2004). *Phys. Rev. B*, **69**, 035411.
Ridgway, M. C., Azevedo, G. de M., Glover, C. J., Elliman, R. G., Llewellyn, D. J., Cheung, A., Johannessen, B., Brett, D. A. & Foran, G. J. (2004). *Nucl. Instrum. Methods Phys. Rev. Sect. B*, **218**, 421–426.
Ridgway, M. C., Yu, K. M., Glover, C. J., Foran, G. J. & Clerc, C. (1999). *Phys. Rev. B*, **60**, 10831–10836.
Rockenberger, J., Tröger, L., Kornowski, A., Vossmeyer, T., Eychmüller, A., Feldhaus, J. & Welle, H. (1997). *J. Phys. Chem. B*, **101**, 2691–2701.
Rockenberger, J., Tröger, L., Rogach, A. L., Tischer, M., Grundmann, M., Eychmüller, A. & Weller, H. (1998). *J. Chem. Phys.* **108**, 7807–7815.
Sun, Z., Wei, S., Kolobov, A. V., Oyanagi, H. & Brunner, K. (2005). *Phys. Rev. B*, **71**, 245334.
Tsoukalas, D., Dimitrakis, P., Kolliopoulou, S. & Normand, P. (2005). *Mater. Sci. Eng. B*, **124–125**, 93–101.
Vincent, B., Damlencourt, J. F., Rivallin, P., Nolot, E., Licitra, C., Morand, Y. & Clavelier, L. (2007). *Semicond. Sci. Technol.* **22**, 237–244.
Wagner, V. C. (1961). *Z. Elektrochem.* **65**, 581–591.
Waseda, Y. (2002). *Anomalous X-ray Scattering for Materials Characterization*. Berlin: Springer.
Wertheim, M. S. (1963). *Phys. Rev. Lett.* **10**, 321–323.
Yonenaga, I. & Sakurai, M. (2001). *Phys. Rev. B*, **64**, 113206.
Zabinsky, S. I., Rehr, J. J., Ankudinov, A., Albers, R. C. & Eller, M. J. (1995). *Phys. Rev. B*, **52**, 2995–3009.
Zhang, B., Shrestha, S., Green, M. A. & Conibeer, G. (2010). *Appl. Phys. Lett.* **96**, 261901.